

System-Level DC-to-DC Analysis and Experiments of Ultrasonic Power Transfer Through Metallic Barriers

Ahmed Allam , Christian L. Arrington, Christopher St. John, Jeffrey Steinfeldt, Alper Erturk , and Ihab El-Kady

Abstract—Ultrasonic waves can be used to transfer power through sealed metallic enclosures when feedthrough wires are not a viable or desirable option. In this work, we present a complete system-level investigation of ultrasonic power transfer through metallic barriers via detailed experiments, analytical modeling, and numerical simulations for analyzing and predicting the dc-to-dc performance. A Class E amplifier design is tightly integrated with the ultrasonic system to excite it efficiently, and a full-bridge rectifier converts its output to dc. A 1-D transfer matrix model was used to model the ultrasonic system, and a harmonic balance analysis simulated the coupled response, including the driving and rectifying electronics. The analytical results are compared to numerical simulations using the finite element method and experimental measurements. The developed system achieves an 83% ac-to-ac efficiency through a 3 mm aluminum barrier while operating at 1 MHz. The system's overall dc-to-dc efficiency peaked at 68% while delivering 17.5 W to a dc load.

Index Terms—Piezoelectric devices, power amplifiers, ultrasonic transducers, wireless power transmission.

I. INTRODUCTION

SENSITIVE electronics are commonly sealed in metallic enclosures to shield them from electromagnetic interference. Any gaps or slots in the enclosure result in electromagnetic leakage and reduce the shielding performance. Physical gaps are also undesirable to ensure the structural integrity of the metallic enclosure, such as for sending power to electronics placed on the external surface of an aircraft, spacecraft, or submarine.

Manuscript received 16 January 2022; revised 19 June 2022; accepted 30 July 2022. Recommended by Technical Editor J. Hey and Senior Editor X. Tan. (Corresponding author: Ahmed Allam.)

Ahmed Allam and Alper Erturk are with the G. W. Woodruff School of Mechanical Engineering, Georgia Institute of Technology, Atlanta, GA 30332 USA (e-mail: a.allam@gatech.edu; alper.erturk@me.gatech.edu).

Christian L. Arrington, Christopher St. John, Jeffrey Steinfeldt, and Ihab El-Kady are with the Photonic and Phononic Microsystems Department, Sandia National Laboratories, Albuquerque, NM 87123 USA (e-mail: clarrin@sandia.gov; cstjohn@sandia.gov; jsteinf@sandia.gov; ielkady@sandia.gov).

Color versions of one or more figures in this article are available at <https://doi.org/10.1109/TMECH.2022.3195973>.

Digital Object Identifier 10.1109/TMECH.2022.3195973

Ultrasonic waves have, thus, been investigated to transmit power and data through metallic barriers [1]. Ultrasonic power transfer (UPT) can also supply power to sensors placed in sealed hazardous environments, such as nuclear waste containers. The ability to send power through metals allows for using continuous structures for sealing the hazard and eliminates the risk associated with battery replacement. Weather protection and waterproofing are among other benefits of UPT, as charging ports introduce the risk of water damage.

Piezoelectric transducers are widely used to generate [2], [3] and harvest [4], [5] mechanical waves and vibrations. They were first used by Hu et al. [6] to transmit power through metals using ultrasonic waves. Since then, multiple research groups have investigated using piezoelectric transducers for UPT, albeit with different motivations. The NASA Jet Propulsion Laboratory explored supplying high power through titanium barriers for space exploration applications [7]. They powered a 100 W incandescent lamp with a peak ultrasonic efficiency of 88% using air-backed piezoelectric transducers operating at 750 kHz [8]. They later demonstrated 1 kW of power transfer with 84% ultrasonic efficiency utilizing a pair of Tonpliz transducers operating at 25 kHz [9]. Researchers from the Rensselaer Polytechnic Institute focused on simultaneously transmitting power and data through thick steel barriers (submarine steel) [10], [11]. They demonstrated simultaneous 50 W (@1 MHz) power transfer and 17.37 Mb/s (@4 MHz) data transfer using two separate transducers mounted on the same 2.5"-thick steel wall [12]. They also tested the power transfer limits using 2.5 cm diameter piezoelectric tiles operating at 1 MHz and demonstrated 141 W power transfer with an ultrasonic efficiency of 67% before failure [13].

Most of the surveyed through-metal UPT literature only reported the measured ultrasonic (ac-to-ac) efficiency from simulations [6], [8], [14]–[16] or experiments [7], [13], [17], [18]. Attempts to compare experimental to simulated ac-to-ac efficiency showed significant discrepancies [19], [20]. Moreover, only a few publications discussed the efficiency of the system with energy harvesting electronics. Lawry et al. [12], Yang et al. [21], and Tseng et al. [22] reported the ac-to-dc efficiency by incorporating a full-bridge rectifier in their experiments; however, they did not report the overall dc-to-dc efficiency, which includes the driving electronics.

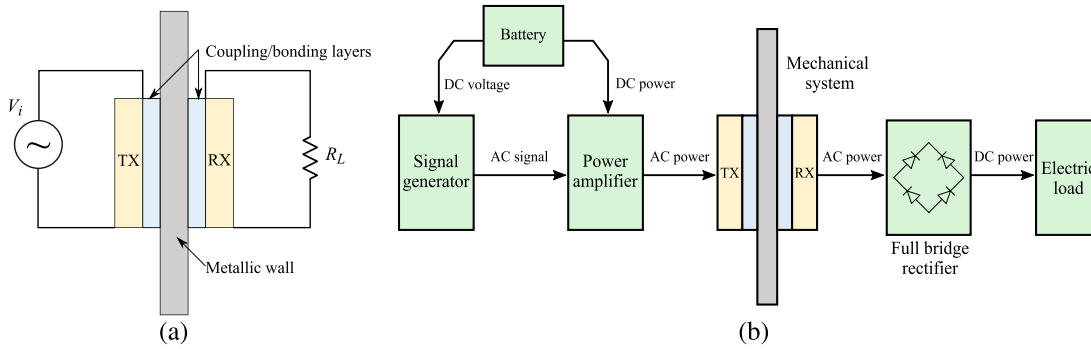


Fig. 1. (a) Basic configuration of an ac-to-ac through-metal UPT system. (b) Block diagram showing the essential components for a dc-to-dc UPT system.

In this article, the overall performance of a dc-to-dc UPT system is analyzed. The ultrasonic system is simulated analytically using the transfer matrix method and numerically using the finite element method (FEM), then verified experimentally. The ac-to-ac performance of the system is reported for multiple transducer sizes and barrier thicknesses, highlighting the factors affecting the ac efficiency. A class E power amplifier is then designed to be tightly integrated with the ultrasonic system by leveraging it as a mechanical filter. The system's dc-to-dc performance, including the amplifier and a full-bridge rectifier, is simulated using the harmonic balance (HB) method and verified experimentally. The end-to-end efficiency and dc power output of the system are analyzed for several dc supply voltages.

II. ANALYTICAL MODELING

A simplified representation of a through-metal power transfer system is shown in Fig. 1(a). It consists of transmitting and receiving piezoelectric disc transducers with the metallic wall in the middle. The transducers can be mounted on the metallic wall using glue (epoxy, polyurethane, cyanoacrylate) or a coupling gel (glycerin, honey, ultrasound gel). The accurate modeling of the coupling (bonding) layer is essential since it strongly influences power transmission, especially at higher frequencies. The transmitter is connected to a power source capable of applying a voltage V_i , while the receiver is connected to a resistive load R_L . For high-frequency systems similar to the one considered in Fig. 1, the lateral dimensions of the transducer are usually much larger than its thickness, which allows for assuming 1-D propagation of ultrasonic waves from the transmitter to the receiver and neglecting lateral propagating waves. The validity of this approximation for the base model is assessed in Section III-C.

Transmission line models (1-D waveguide models) are commonly used for predicting the behavior of 1-D ultrasonic systems [15], [23], [24]. These models are typically valid for frequencies above 100 kHz, where the wavelength of the propagating waves is smaller than the thickness of the metallic wall. For low-frequency systems operating below 100 kHz, lumped parameter models and lumped circuit elements are more appropriate [25], [26] since the wavelength becomes much longer than the system's dimensions.

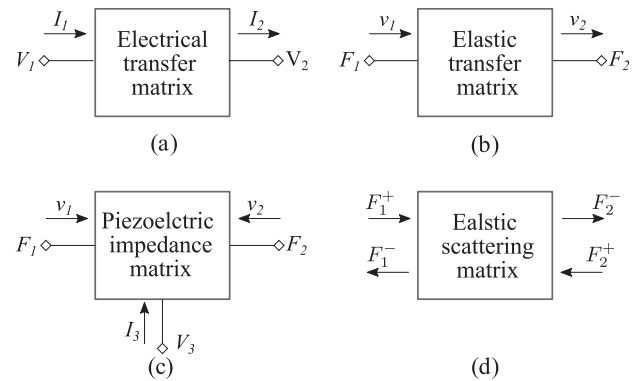


Fig. 2. Transfer matrix parameters for (a) elastic layer and (b) electrical circuit. (c) Impedance matrix representation for a piezoelectric transducer. (d) Scattering matrix representation for an elastic layer.

A 1-D ultrasonic system can be modeled as a series of cascaded elastic/acoustic layers representing different system components. Each elastic layer is modeled as a two-port element with a 2×2 matrix relating the acoustic pressure and velocity at each port. Among the different representations that can be used for modeling two-port elements (S -parameters, Z -parameters, Y -parameters, and others), the transfer matrix [also known as ABCD parameters in the radiofrequency (RF) literature] simplifies the algebraic manipulations needed to solve the system. The transfer matrix relates the force and velocity at the input of a layer F_1, v_1 to the output F_2, v_2 by

$$\begin{bmatrix} F_1 \\ v_1 \end{bmatrix} = \mathbf{T} \begin{bmatrix} F_2 \\ v_2 \end{bmatrix}, \quad \mathbf{T} = \begin{bmatrix} T_{11} & T_{12} \\ T_{21} & T_{22} \end{bmatrix} \quad (1)$$

where velocity directions are shown in Fig. 2(a). The elastic transfer matrix is analogous to the electric transfer matrix [see Fig. 2(b)], with forces replaced by applied voltages and velocities by electric currents.

For an ultrasonic system consisting of n cascaded layers, the transfer matrix of the overall system T_{sys} is calculated by multiplying layer matrices

$$\mathbf{T}_{\text{sys}} = \mathbf{T}_1 \mathbf{T}_2 \dots \mathbf{T}_n. \quad (2)$$

The transfer matrix of a passive elastic layer with acoustic impedance Z_n and thickness h_n can be calculated from the

relation

$$\mathbf{T}_n = \begin{bmatrix} \cos(k_n h_n) & jZ_n A_n \sin(k_n h_n) \\ j \frac{\sin(k_n h_n)}{Z_n A_n} & \cos(k_n h_n) \end{bmatrix} \quad (3)$$

where $k_n = \omega/c_n$ is the wavenumber of the ultrasonic wave in layer n , c_n is the speed of sound in the layer, and A_n is the surface area of the layer. Equation (3) could be used to calculate the transfer matrices for the metallic wall and bonding layers shown in Fig. 1(a).

The piezoelectric layers, on the other hand, cannot be represented directly as a 2-port transfer matrix since they possess a third electrical port in addition to the two mechanical ports and are, thus, represented as a 3-port element [see Fig. 2(c)]. For a thin piezoelectric layer, the electrical and mechanical equations of motion can be cast into the impedance matrix (Z -parameters) form as [27]

$$\begin{bmatrix} F_1 \\ F_2 \\ V_3 \end{bmatrix} = \mathbf{Z}_p \begin{bmatrix} v_1 \\ v_2 \\ I_3 \end{bmatrix}$$

$$\mathbf{Z}_p = -j \begin{bmatrix} Z_p \cot(k_p h_p) & Z_p \csc(k_p h_p) & \frac{\bar{h}_{33}}{\omega} \\ Z_p \csc(k_p h_p) & Z_p \cot(k_p h_p) & \frac{\bar{h}_{33}}{\omega} \\ \frac{\bar{h}_{33}}{\omega} & \frac{\bar{h}_{33}}{\omega} & \frac{1}{\omega C_p} \end{bmatrix} \quad (4)$$

where $Z_p = \rho_p c_p A_p$ is the mechanical impedance of the piezoelectric layer, ρ_p is the density, $\bar{h}_{33} = e_{33}/\epsilon_{33}^s$ is known as the transmitting coefficient, e_{33} is the piezoelectric voltage constant, ϵ_{33}^s is the permittivity at constant strain, $k_p = \omega/c_p$ is the wavenumber in the piezoelectric layer, and $C_p = \epsilon_{33}^s A_p/h_p$ is the piezoelectric layer capacitance at constant strain (when mechanically clamped). The directions for the velocities and electric currents used to deduce the impedance matrix in (4) are defined in Fig. 2(c).

Assuming that the acoustic impedance Z_b at the transducer's backside is known, (4) can be reduced to the transfer matrix form by substituting the relation

$$F_2 = -Z_b A_p v_2. \quad (5)$$

This yields the transfer matrix for a piezoelectric layer operating as a receiver

$$\mathbf{T}_r = \begin{bmatrix} C/A & D - BC/A \\ 1/A & -B/A \end{bmatrix} \quad (6)$$

where

$$\begin{aligned} A &= Z_{31} - \frac{Z_{32}Z_{21}}{Z_b + Z_{22}}, & B &= \frac{Z_{32}Z_{23}}{Z_b + Z_{22}} - Z_{33} \\ C &= Z_{11} - \frac{Z_{12}Z_{21}}{Z_b + Z_{22}}, & D &= \frac{Z_{12}Z_{23}}{Z_b + Z_{22}} - Z_{13} \end{aligned} \quad (7)$$

and Z_{ij} are elements of the piezoelectric impedance matrix given in (4).

The transfer matrix for a layer operating as a transmitter is given by

$$\mathbf{T}_t = \begin{bmatrix} B/D & BC/D - A \\ -1/D & -C/D \end{bmatrix}. \quad (8)$$

Equation (8) is not simply the matrix inverse of the receiver as the mechanical and electrical ports are reversed.

For power transfer applications, the piezoelectric layer's backside is typically left exposed to air ($Z_b \approx 0$) since air's mechanical impedance is much lower than piezoelectric materials, and thus, virtually no power is lost through the transducer's backside.

The equivalent transfer matrix for the system shown in Fig. 1(a) can be calculated by multiplying transfer matrices of the cascaded layers

$$\mathbf{T}_{\text{sys}} = \mathbf{T}_t \mathbf{T}_b \mathbf{T}_w \mathbf{T}_b \mathbf{T}_r \quad (9)$$

where $\mathbf{T}_b, \mathbf{T}_w$ are the transfer matrices for the bonding layers and the metallic wall, respectively.

A. Modeling of Attenuation

Accurately modeling attenuation is crucial for estimating the efficiency of UPT systems; however, attenuation is a complex phenomenon with several contributing factors even in a homogeneous medium. Attenuation is also frequency-dependent in most materials, which further complicates its characterization and reporting in the literature. Attenuation in solids is still an active research area with multiple theories for damping mechanisms, unlike the attenuation mechanisms in liquids and gases, which can be derived from basic principles [28].

A phenomenological approach for defining attenuation involves defining a complex wavenumber [29]

$$k = \omega/c - j\alpha(\omega) \quad (10)$$

where α is a frequency-dependent attenuation coefficient in Np/m; however, it is commonly reported with the units dB/mm.

In low-frequency vibrations, mechanical (structural or hysteretic) damping is commonly represented as a mechanical loss factor (η_m). The loss factor η_m is defined by considering a complex elasticity matrix to represent hysteretic damping in a material¹

$$\bar{\mathbf{C}} = \mathbf{C}(1 + j\eta_m). \quad (11)$$

The quality factor $Q_m = 1/\eta_m$ is also used in some conventions. A relation between η_m and α can be derived from the complex wavenumber

$$\alpha = -\text{Im} \left\{ \frac{\omega}{c\sqrt{1 + j\eta_m}} \right\}. \quad (12)$$

For small values of η_m , the binomial approximation $\frac{1}{\sqrt{1 + j\eta_m}} \approx 1 - j\frac{\eta_m}{2}$ can be used to further simplify the relation to

$$\alpha = \frac{\omega\eta_m}{2c} = \frac{\pi\eta_m f}{c}. \quad (13)$$

Equation (13) assumes a linear frequency dependence for attenuation, and represents a good approximation for attenuation in

¹Note that η_m is sometimes referred to as the mechanical loss tangent ($\tan \delta_m$).

many solids at frequencies below 5 MHz as demonstrated by the notable work of Ono [29].

A more generalized form is necessary to describe complex damping behavior and other damping models such as composite and porous materials. This form is usually a polynomial in frequency defined as [29]

$$\alpha = \sum C_n f^n \quad (14)$$

where C_n are the attenuation coefficients commonly given in the units [dB/m/MHzⁿ], and n are integer or rational exponents used to fit attenuation measured experimentally. Equation (14) is a generalized representation of various damping models such as quadratic dependence on frequency ($\alpha = C_2 f^2$) derived by assuming attenuation proportional to the strain rate in the material [30], [31].

Piezoelectric transducers have additional attenuation mechanisms that arise from the coupling between the electrical and mechanical domains. In addition to mechanical attenuation commonly reported as a mechanical quality factor (Q_m), energy is dissipated in piezoelectric transducers due to dielectric and piezoelectric losses. Dielectric losses are commonly reported with a dielectric loss tangent ($\tan \delta_e$), yielding a complex permittivity matrix ($\bar{\epsilon}$)

$$\bar{\epsilon} = \epsilon(1 - j \tan \delta_e). \quad (15)$$

Piezoelectric losses are usually difficult to distinguish from mechanical and dielectric losses [32], and hence, they are commonly accounted for in the mechanical and dielectric loss factors rather than reported separately.

B. Performance Metrics

The performance of through-metal UPT systems will be assessed from the voltage transfer function ($V_{\text{out}}/V_{\text{in}}$) and the power transfer efficiency. These parameters can be calculated from \mathbf{T}_{sys} , (9), and the electrical load Z_L connected to the output of the system. The input and output voltages and currents to the ultrasonic system are related by

$$\begin{bmatrix} V_{\text{in}} \\ I_{\text{in}} \end{bmatrix} = \mathbf{T}_{\text{sys}} \begin{bmatrix} V_{\text{out}} \\ I_{\text{out}} \end{bmatrix}, \quad \mathbf{T}_{\text{sys}} = \begin{bmatrix} T_{11} & T_{12} \\ T_{21} & T_{22} \end{bmatrix}. \quad (16)$$

By substituting load impedance relation $V_{\text{out}} = Z_L I_{\text{out}}$ into (16) and assuming a known voltage V_{in} is applied to the system, we arrive to

$$\begin{aligned} V_{\text{out}} &= \frac{V_{\text{in}} Z_L}{T_{11} Z_L + T_{12}}, & I_{\text{out}} &= \frac{V_{\text{in}}}{T_{11} Z_L + T_{12}} \\ I_{\text{in}} &= \frac{T_{21} Z_L + T_{22}}{T_{11} Z_L + T_{12}} V_{\text{in}}. \end{aligned} \quad (17)$$

The voltage frequency response function (FRF), also known as the voltage transfer function or voltage gain of the ultrasonic system, can be calculated from (17) as

$$\frac{V_{\text{out}}}{V_{\text{in}}} [dB] = 20 \log_{10} \left(\frac{Z_L}{T_{11} Z_L + T_{12}} \right). \quad (18)$$

TABLE I
MATERIAL PROPERTIES USED IN THE TRANSDUCER 1-D MODEL

Property	ρ_p	c_p	\bar{h}_{33}	C_{33}^D	C_p	Q_m	$\tan \delta_e$
Unit	kg/m ³	m/s	kV/mm	GPa	nF	-	%
Value	7900	4706	2594	175	1.9	500	0.4

The real input and output power (P_{in} and P_{out}) to the system are calculated from

$$P_{\text{in}} = \frac{1}{2} \text{re}(V_{\text{in}} I_{\text{in}}^*), \quad P_{\text{out}} = \frac{1}{2} \text{re}(V_{\text{out}} I_{\text{out}}^*) \quad (19)$$

where * indicates the complex conjugate.

The operating ac-to-ac efficiency of the ultrasonic system (η_{AC}) is defined as the ratio of the ac electrical power consumed by the electric load to the ac electric power input to the ultrasonic system. It does not account for the electrical power reflected to the power source by the ultrasonic system due to impedance mismatch. The ac-to-ac ultrasonic efficiency is given by

$$\eta_{\text{AC}} = \frac{P_{\text{out}}}{P_{\text{in}}} \times 100\%. \quad (20)$$

III. BENCHMARK SYSTEM PERFORMANCE

The implementation of the through-metal UPT shown in Fig. 1(a) is discussed first to establish the practical model geometry and physical parameters. The performance of the system is then characterized analytically, numerically using the FEM, and experimentally. The performance of the 1-D analytical model is compared to 2-D FEM model predictions and experimental results to assess the validity of the 1-D approximations for the considered system.

A. Experimental Validation

A piezoelectric transducer with a radius of 15 mm and a thickness of 2.1 mm, supplied by Steiner & Martins Inc., is selected as a compromise between:

- 1) maximizing the directivity of the transducer to minimize energy lost to lateral propagation;
- 2) minimizing the attenuation by keeping the frequency as low as practically possible;
- 3) keeping the impedance of the transducer close to 50 Ω to ensure compatibility with commercial RF equipment;
- 4) keeping the dimensions of the transducer reasonably small.

The transducer material is a hard PZT ceramic (PZT-4/SM111), which has a high quality factor compared to other piezoelectric ceramics, thus minimizing the power dissipated in the transducer. The reduced properties for the 1-D piezoelectric transducer are summarized in Table I. An anodized aluminum wall is used in the experiment (see Fig. 3) to limit electrical cross-talk between the piezoelectric tiles that might interfere with the measurement. A thin layer of gold is deposited on the aluminum wall to facilitate the electrical connection to the bonded electrode. The transducer is then bonded to the aluminum wall using epoxy in a vacuum bonding procedure

overall response of the system with global peaks at odd multiples of the thickness resonance of the transducer seen around 1.1, 3.3, 5.5, and 7.7 MHz. The voltage FRF is minimum around 2.2, 4.4, 6.6, and 8.8 MHz, since the electrical and mechanical domains do not couple at the even modes of piezoelectric transducers [27], [33]. Using a thinner transducer would shift these global peaks to higher frequencies and increase the interval between them.

The second class of resonances originates from the standing waves in the aluminum wall (frequencies at which the thickness of the wall is an integer multiple of the pressure waves traveling through it). The sharpness of these resonance peaks depends on the impedance mismatch between the metal and the piezoelectric domain. The frequency interval of these peaks depends mainly on the thickness of the aluminum wall, with thicker walls resulting in smaller intervals.

The third class of resonances is related to higher order radial modes in the transducers, and as shown in the insets of Fig. 5, they appear as a noisy response around the fundamental frequency of the transducer. The strength of these modes depends on the aspect ratio of the transducer, and their effect diminishes for higher odd multiples of the transducer resonance.

D. Maximum Achievable Efficiency

The main factor that defines the efficiency of the 1-D ultrasonic system model is the attenuation present in the system. For a lossless system, the operating efficiency is 100% regardless of other properties, and hence, the attenuation value is critical to reliably predict the efficiency. Given the inevitable attenuation in the system, internal reflections contribute to the degradation of the system efficiency. When the impedance of all the UPT domains is well-matched, the ultrasonic waves travel once through the domain without reflection experiencing minimum attenuation. The presence of impedance mismatches causes multiple internal reflections in each layer, and thus, the traveling wave experiences additional attenuation each time it is reflected back and forth in the system, which reduces the efficiency.

The amount of reflection at an interface between two domains is captured by the scattering matrix, which relates incident waves (voltage or force) to the reflected and transmitted waves. For a two-port domain, the scattering matrix is defined as

$$\begin{bmatrix} F_1^- \\ F_2^- \end{bmatrix} = \begin{bmatrix} S_{11} & S_{12} \\ S_{21} & S_{22} \end{bmatrix} \begin{bmatrix} F_1^+ \\ F_2^+ \end{bmatrix} \quad (21)$$

where F_1^+ and F_2^+ are the complex incident force (pressure) on ports 1 and 2 of the system, and F_1^- and F_2^- are the pressure coming out of the system, as shown in Fig. 2(d). The scattering matrix can also be defined for voltage signals (V^+ , V^-) depending on whether the domain port is electrical or mechanical. The elements of the scattering matrix can be calculated from the transfer matrix [34]. S_{11} and S_{22} represent the complex reflection coefficients of ports 1 and 2, respectively, while S_{12} and S_{21} are the complex transmission coefficients.

The UPT system efficiency is limited by the following two mechanisms: 1) the attenuation of the different elements as the waves propagate from the source to the load, and 2) wave reflection between the system components. While attenuation

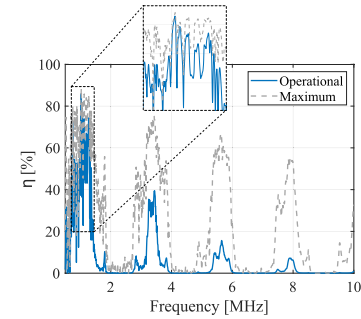


Fig. 6. AC-to-AC efficiency obtained numerically compared to the maximum achievable efficiency calculated using (22).

is an inherent property of the materials used and can only be enhanced by using lower loss materials, losses due to reflection can be reduced by matching the system's input and output impedance to the source and load impedance. It can also be reduced by matching the impedance between the different elastic layers. However, acoustic matching layers might introduce additional attenuation to the system which might be larger than the reduction due to reflection losses.

The maximum achievable ac efficiency occurs when the reflections at the input and output of the system are minimized. This maximum efficiency can be calculated by determining the impedance at the system's input and output needed to minimize the reflections (simultaneous conjugate matching). This efficiency only depends on the system parameters and could be calculated using the relation [35]

$$\eta_{\max} = \frac{1}{1 - |\Gamma_S|^2} |S_{21}|^2 \frac{1 - |\Gamma_L|^2}{|1 - S_{22}\Gamma_L|} \times 100\% \quad (22)$$

where the matched source and load reflection coefficients (Γ_S , Γ_L) are given by

$$\Gamma_S = \frac{B_1 \pm \sqrt{B_1^2 - 4|C_1|^2}}{2C_1}, \quad \Gamma_L = \frac{B_2 \pm \sqrt{B_2^2 - 4|C_2|^2}}{2C_2} \quad (23)$$

where

$$B_1 = 1 + |S_{11}|^2 - |S_{22}|^2 - |\Delta|^2 \quad (24)$$

$$B_2 = 1 + |S_{22}|^2 - |S_{11}|^2 - |\Delta|^2 \quad (25)$$

$$C_1 = S_{11} - \Delta S_{22}^* \quad (26)$$

$$C_2 = S_{22} - \Delta S_{11}^* \quad (27)$$

$$\Delta = S_{11}S_{22} - S_{12}S_{21}. \quad (28)$$

The matched source and load impedance (Z_S^{opt} , Z_L^{opt}) can be calculated from

$$Z_{S,L}^{\text{opt}} = 50 \frac{1 + \Gamma_{S,L}}{1 - \Gamma_{S,L}}. \quad (29)$$

It should be noted that Freychet et al. [15] calculated the maximum achievable efficiency and corresponding matching source and load impedance using the elements of the system's impedance matrix which should yield identical results to (22).

Fig. 6 shows the maximum achievable efficiency for the benchmark system compared to the operational efficiency. The

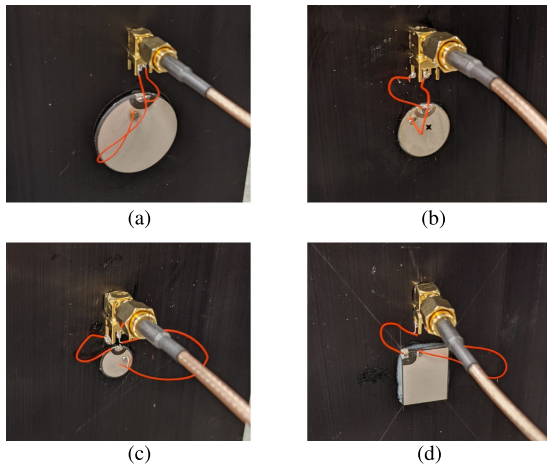


Fig. 7. Experimental setup for through-metal UPT systems using circular transducers with dimensions (a) 30 mm \times 2.1 mm, (b) 15 mm \times 1 mm, (c) 10 mm \times 0.5 mm, and (d) rectangular transducer with dimensions 20 mm \times 15 mm \times 2.1 mm.

operational efficiency is obtained when the receiver is terminated with a 50 Ω resistor. The results show that the peak operational efficiency of the system (at 1.025 MHz) is very close to the maximum achievable efficiency, which means that the system is closely matched to 50 Ω at this frequency. The peak of the maximum achievable efficiency is inversely proportional to the frequency since it is only limited by the attenuation present in the system. However, the difference between the maximum and operational efficiency is significant at higher frequencies, indicating that the impedance mismatch is large. Electrical impedance matching can, thus, enhance the efficiency around the higher transducer resonance frequencies (i.e., 3.3, 5.5, and 7.7 MHz).

IV. TRANSDUCERS WITH WRAPAROUND ELECTRODES

Transducers with wraparound electrodes, as shown in Fig. 7, allow for easy electrical access to the bonded side of the transducer without using the metallic wall as a common electrical connection. However, the wraparound electrode portion of the transducer does not contribute to the active area of the transducer and introduces asymmetries in the active transducer geometry which might excite additional lateral modes limiting the efficiency of the structure. This section investigates four transducers with wraparound electrodes and different shapes, thicknesses, and areas. Their performance is also compared to the base model, which uses transducers with full coverage electrodes.

An anodized aluminum plate with a thickness of 1/4" (6.35 mm) is considered, and a pair of transducers are bonded at the center of the plate as shown in Fig. 7. Three circular SM111 transducers with dimensions of 30 mm \times 2.1 mm (the same as the base model), 15 mm \times 1 mm, and 10 mm \times 0.5 mm are considered as well as a rectangular transducer with dimensions of 20 mm \times 15 mm \times 2.1 mm.

The voltage FRF and operating efficiency are shown in Fig. 8. Since the plate used for this set of experiments is twice the thickness of that used in the base model, the wall resonances visible in Fig. 8(a) are closer in frequency than Fig. 5(a). For the

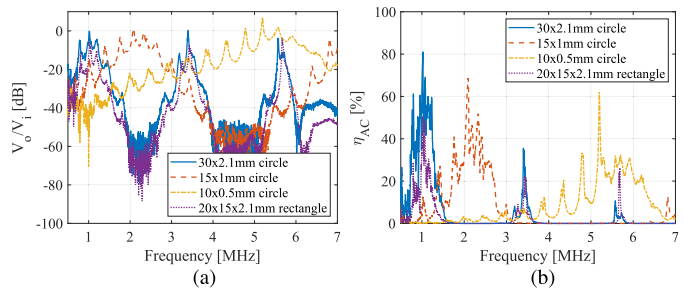


Fig. 8. Experimental (a) voltage FRF and (b) AC-to-AC efficiency for UPT systems for the transducers shown in Fig. 7.

30 mm \times 2.1 mm (1 MHz) transducer, the peak efficiency (80% as shown in Fig. 8) is only slightly lower than that observed in the base model (83%) using the same transducer dimensions [see Fig. 8(b)]. The transducer used in the base model had full coverage electrodes suggesting that wraparound electrodes have a limited effect on the efficiency when the transducers are correctly aligned. On the other hand, the rectangular transducers had the wraparound part of the electrode at the corner as shown in Fig. 7(d) preventing aligning the wraparound part of the transmitting and receiving transducer. The wraparound electrode misalignment, general transducer misalignment, and other corner effects reduced the peak efficiency compared to the circular tiles (50% for the rectangular tiles versus 80% for the circular tiles).

The results for the higher frequency tiles show the expected trend of reduction in efficiency as the frequency of operation increases. The smaller transducers are also more sensitive to misalignment, which most likely contributed to the reduced operating efficiency. As shown in Fig. 8(b), the 15 mm \times 1 mm (2 MHz) and 10 mm \times 0.5 mm (5 MHz) transducers showed a peak efficiency of 67% and 61%, respectively. The peak efficiency obtained by a thin transducer around its resonance (10 mm \times 0.5 mm transducer, for example) is larger than that obtained by using the higher order modes of a thicker transducer (third mode of the 30 mm \times 2.1 mm transducer).

V. INTERFACING CIRCUITS

For a working implementation of a UPT system, it is necessary to consider the interfacing electronics in addition to the ultrasonic system itself. The essential components for a minimal functional UPT system are shown in Fig. 1(b). Electric power is commonly available in dc form either directly from a battery or through rectified ac mains. The dc power is converted to an RF signal to excite the ultrasonic system at the peak efficiency/power transfer frequency. The RF signal is supplied from a signal generation circuit connected to drive a power amplifier circuit designed to operate efficiently at the system frequency.

Typical driving and rectifying circuits include nonlinear components, such as transistors and diodes. Therefore, a nonlinear circuit solver is needed for characterizing the overall performance of the system. Since UPT systems are modeled and characterized in the frequency domain, a nonlinear HB solver is better suited for simulating the system than commonly used time-domain-based software, such as SPICE or SIMULINK.

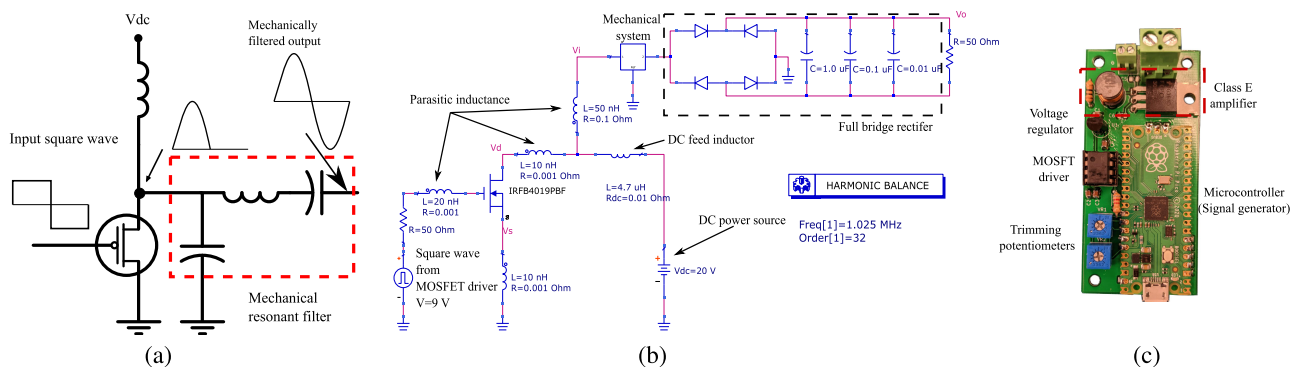


Fig. 9. (a) Concept and (b) simulation of the proposed class E amplifier with the mechanical system acting as the resonant filter. The mechanical system block represents the base model shown in Fig. 1(a). (c) Implemented printed circuit board which includes the designed class E power amplifier, a microcontroller used as a variable square wave generator, and the MOSFET driving circuits.

The HB method directly solves for the steady-state system response at the fundamental frequency of excitation and its harmonics, which is usually faster than simulating many time steps before the time-domain solver reaches steady-state operation [36].

A. Class E Amplifier Design for UPT

This section investigates the design of class E power amplifiers for operation with piezoelectric UPT systems. We suggest a design that relies on the resonant mechanical system to double as the filtering circuit of the amplifier. The integration of the mechanical system in the amplifier design reduces the required electrical power components to a single feed inductor connected to the dc power supply.

Class E power amplifiers traditionally rely on a resonant circuit [see Fig. 9(a)] to provide the transient response required for the amplifier's operation. The resonant circuit filters the square wave driving signal to generate an output sinusoidal signal. Since piezoelectric UPT systems are resonant and capacitive, the mechanical system could provide the transient response required for the operation of the amplifier, and the harmonics generated are filtered mechanically, providing a clean sinusoidal output at the piezoelectric receiver. This tight integration, however, requires a coupled electromechanical model for optimizing the operation of the amplifier.

A coupled electromechanical HB circuit simulation is constructed to design the proposed amplifier using keysight advanced design system (ADS) software, as shown in Fig. 9(b). The dynamics of the mechanical system are exported from the FEM model as a touchstone file (S -parameters representation) and then imported into ADS, as indicated in Fig. 9(b). A FQP30N06 power MOSFET is selected for the design because of its low on resistance ($R_{DS} = 40 \text{ m}\Omega$) and fast switching time ($t_{on}^{(max)} = 210 \text{ ns}$). The feed inductor is tuned to provide zero-voltage switching (ZVS) conditions at the peak efficiency frequency of the mechanical system (1.025 MHz). The parasitic inductance from the TO-220 package of the MOSFET and the connecting wires are included in the model.

A Raspberry Pi Pico microcontroller provides a programmable square wave signal to the power amplifier circuit,

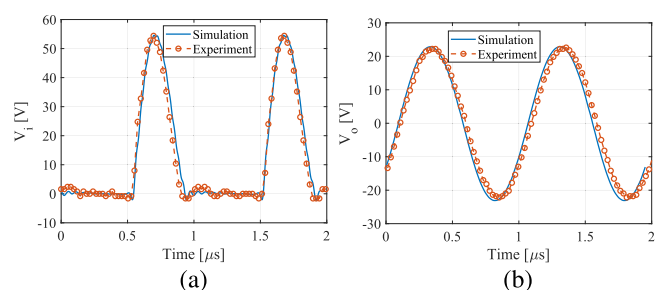


Fig. 10. Simulated and experimental (a) input and (b) output voltage waveforms to and from the ultrasonic system as supplied from the designed power amplifier. The simulation results are obtained from the circuit shown in Fig. 9(b) without a full-bridge rectifier.

as shown in Fig. 9(c). The microcontroller is connected to a UCC27423P high-speed MOSFET gate driver integrated circuit (IC). The square wave signal's frequency and duty cycle are controlled using two trimming potentiometers connected to the analog inputs of the microcontroller, as shown in Fig. 9(c). The circuit is designed to operate with 5–15 V dc supply levels allowing for direct operation from a single 9 V alkaline battery or a 7.2 V lithium-ion battery pack.

VI. UPT WITH AN INTEGRATED POWER AMPLIFIER (DC-TO-AC OPERATION)

The performance of the UPT system with an integrated class E amplifier is evaluated as follows. The input and output voltage waveforms are shown in Fig. 10 for a 50Ω resistive load without the bridge rectifier. A 12 V power supply is used to drive the circuit, and an excellent match is observed between the experimental measurements and the simulated waveforms. In Fig. 10(a), the input voltage is zero when the MOSFET is ON (in the time interval between 0 and $0.5 \mu\text{s}$). It swings sinusoidally when the MOSFET is switched OFF. The output of the system is a mechanically filtered sinusoidal signal, as shown in Fig. 10(b).

For efficient operation of class E power amplifiers, a ZVS condition must be achieved, which depends on the mechanical system properties, operating frequency, driving circuit duty cycle, and the feed inductance value. Since the frequency and the system properties are fixed, the amplifier is tuned by adjusting

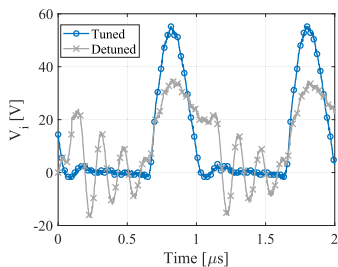


Fig. 11. Experimental amplifier voltage when it is tuned by selecting a proper feed inductor ($4.7 \mu\text{H}$) versus the detuned operation when a different inductor is used ($10 \mu\text{H}$ in the case shown).

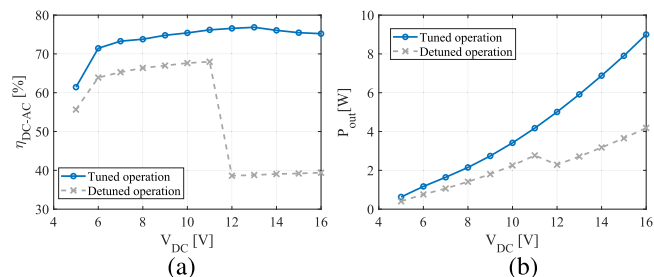


Fig. 12. (a) DC-to-AC experimental system efficiency versus dc input voltage. The efficiency is calculated by dividing ac output power supplied to a 50Ω load by the total input dc power. (b) Output power versus the input dc voltage supplied.

the duty cycle and the feed inductor value. Fig. 11 shows the voltage at the MOSFET drain (input to the ultrasonic system) for a tuned operation when ZVS is achieved versus detuned operation. In the detuned operation, the transistor switches OFF when the drain voltage is not zero, causing high-frequency oscillations due to the parasitic components in the circuit.

In order to quantify the total dc-to-ac efficiency of the UPT system, the input dc voltage to the amplifier is varied from 5 to 16 V, while recording the output power. The dc power supplied to the amplifier circuit (including the microcontroller and driver IC) is measured using an Agilent E3641A dc power supply with a current readout. The efficiency from a dc supply is calculated from

$$\eta_{\text{DC-AC}} = \frac{P_o}{P_{\text{DC}}} \times 100\% \quad (30)$$

where P_o is the output ac power supplied to a 50Ω resistive load and P_{DC} is the total dc power supplied to the system, including the power needed to drive the microcontroller and the gate driving circuit (a constant current of 90 mA).

The total dc-to-ac efficiency is shown in Fig. 12(a) versus the dc supply voltage. The detuned efficiency is also shown in the same figure to highlight the importance of tuning the amplifier. The efficiency of the detuned system drops sharply at 12 V, which is most likely caused by overheating due to inefficient operation. The system shows a peak dc-to-ac efficiency of 77% for tuned operation. The efficiency drops to 60% for lower power transfer because of the overhead of powering the microcontroller and driving circuit. The efficiency of the Class E amplifier at peak dc-to-ac operation (η_{amp}) reached 86.5%, including the

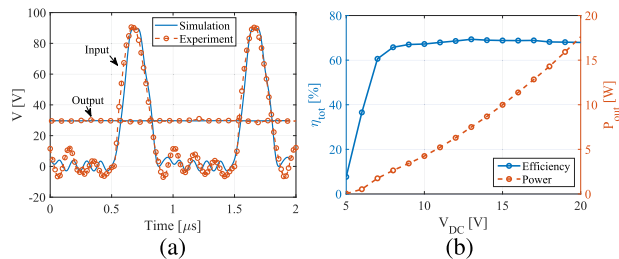


Fig. 13. (a) Simulated and experimental input voltage (V_i) and output voltage (V_o) waveforms [see Fig. 9(b)] of the complete dc-to-dc UPT system operated from a 20 V power supply. (b) Total experimental system efficiency and output power versus dc input voltage.

power needed to drive the amplifier driving circuit. As shown in Fig. 12, the system delivered 9 W of power to a 50Ω load with a 16 V dc input. The system output power is only limited by the breakdown voltage of the MOSFET used and can, thus, deliver more considerable power with a higher rated transistor, as realized in the following section.

VII. OVERALL SYSTEM PERFORMANCE (DC-TO-DC OPERATION)

The full dc-to-dc operation is studied by adding a full-bridge rectifier to the output of the UPT system. Schottky diodes with a fast recovery time are used to minimize the power loss while switching. Capacitors with values of 0.01, 0.1, and $10 \mu\text{F}$ are connected to the output of the rectifier to minimize the output ripple. Multiple capacitors are used to minimize the equivalent series inductance (ESL). The circuit shown in Fig. 9(b) simulates a complete through-metal UPT system that transfers power from a dc source to a dc load. A CDBHM260L-HF full-bridge Schottky rectifier converts the ac output power from the UPT to dc power. The power transistor used in Section VI is upgraded to an IRFB4019PBF power MOSFET capable of handling 150 V to allow for using a larger dc voltage supply. The circuit is implemented experimentally, and the steady-state results are compared to the simulations in Fig. 13(a). An excellent agreement between the simulations and experimental measurement is observed. The experimental results show more oscillations than simulations when the MOSFET is ON (when the input voltage is close to zero) caused by other electrical parasitics not captured by the model. Additionally, the ESL of the smoothing capacitors causes slight ripples in the experimental dc output.

The dc supply voltage to the system is then varied from 5 to 20 V to study its effect on the system efficiency and output power. The total input power from the dc power supply and the output dc power are recorded to calculate the total system efficiency (dc-to-dc) efficiency

$$\eta_{\text{tot}} = \frac{P_{\text{DCo}}}{P_{\text{DCi}}} \times 100\% \quad (31)$$

$$= \eta_{\text{amp}} \eta_{\text{AC}} \eta_{\text{rec}} \quad (32)$$

where η_{rec} is the efficiency of the bridge rectifier. As shown in Fig. 13(b), the dc-to-dc efficiency to a 50Ω load remained

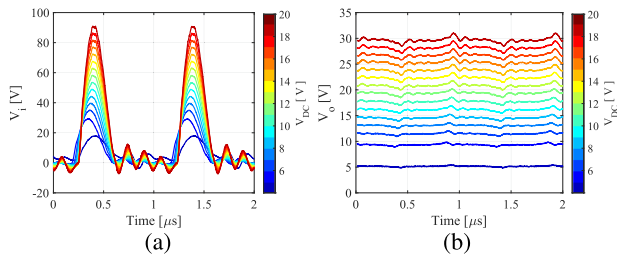


Fig. 14. Experimental (a) input voltage at the amplifier drain and (b) rectified output voltage waveforms on a $50\ \Omega$ load. The waveforms are measured at the dc supply voltage levels shown in the color bar.

constant around 68% for V_{DC} above 8 V. For lower V_{DC} values, the system's efficiency drops quickly due to inefficient amplifier operation. This drop is caused by insufficient MOSFET gate drive voltage and the reduced bridge rectifier efficiency. The system delivered 17.5 W of useful dc power up to the current limit of the dc power supply employed.

The recorded input amplifier drain voltage and dc output voltage waveforms are shown in Fig. 14 for the tested dc supply voltage range. The amplitude of the voltage ripple due to transistor parasitics seems to increase with the supply voltage level. The ripples are caused by a slightly detuned operation of the amplifier, which can be adjusted by using a different dc feed inductor value more suited for the dc-to-dc operation of the system. The ripple of the output dc voltage [see Fig. 14(b)] increases with the amplitude of the output voltage. The UPT system supplied 17.5 W (30 V and 0.59 A) to a $50\ \Omega$ load.

VIII. CONCLUSION

Several configurations for through-metal UPT were developed and experimentally tested. The setup included a bonded transmitter and receiver sending ultrasonic power through an anodized aluminum wall. An efficient class E power amplifier was designed to be tightly integrated into the ultrasonic system with minimal electronic components. The developed amplifier relied on the ultrasonic system for filtering its output signal. A complete power transfer system that includes the amplifier, the ultrasonic setup, and a full-bridge rectifier was simulated and then experimentally verified. An excellent agreement was obtained between the numerical simulations and the experiments. The system delivered 17.5 W of dc power to a $50\ \Omega$ resistive load at a total dc-to-dc efficiency of 68%.

ACKNOWLEDGMENT

Sandia National Laboratories is a multimission laboratory managed and operated by National Technology & Engineering Solutions of Sandia, LLC, a wholly owned subsidiary of Honeywell International Inc., for the U.S. Department of Energy's National Nuclear Security Administration under contract DE-NA0003525. This article describes objective technical results and analysis. Any subjective views or opinions that might be expressed in this article do not necessarily represent the views of the U.S. Department of Energy or the United States Government.

REFERENCES

- [1] D.-X. Yang, Z. Hu, H. Zhao, H.-F. Hu, Y.-Z. Sun, and B.-J. Hou, "Through-metal-Wall power delivery and data transmission for enclosed sensors: A review," *Sensors*, vol. 15, no. 12, pp. 31581–31605, Dec. 2015.
- [2] E. Csencsics and G. Schitter, "Exploring the Pareto fronts of actuation technologies for high performance mechatronic systems," *IEEE/ASME Trans. Mechatronics*, vol. 26, no. 2, pp. 1053–1063, Apr. 2021.
- [3] L. Zheng, W. Chen, D. Huo, and X. Lyu, "Design, analysis, and control of a two-dimensional vibration device for vibration-assisted micromilling," *IEEE/ASME Trans. Mechatronics*, vol. 25, no. 3, pp. 1510–1518, Jun. 2020.
- [4] F. Gao, G. Liu, X. Fu, L. Li, and W.-H. Liao, "Lightweight piezoelectric bending beam-based energy harvester for capturing energy from human knee motion," *IEEE/ASME Trans. Mechatronics*, vol. 27, no. 3, pp. 1256–1266, Jun. 2022.
- [5] H. J. Jung, A. T. Eshghi, and S. Lee, "Structural failure detection using wireless transmission rate from piezoelectric energy harvesters," *IEEE/ASME Trans. Mechatronics*, vol. 26, no. 4, pp. 1708–1718, Aug. 2021.
- [6] Y. Hu, X. Zhang, J. Yang, and Q. Jiang, "Transmitting electric energy through a metal wall by acoustic waves using piezoelectric transducers," *IEEE Trans. Ultrason., Ferroelectr., Freq. Control*, vol. 50, no. 7, pp. 773–781, Jul. 2003.
- [7] S. Sherrit et al., "Studies of acoustic-electric feed-throughs for power transmission through structures," *Proc. SPIE*, vol. 6171, Mar. 2006, Art. no. 617102.
- [8] X. Bao et al., "Wireless piezoelectric acoustic-electric power feedthru," *Proc. SPIE*, vol. 6529, Apr. 2007, Art. no. 652940.
- [9] X. Bao et al., "High-power piezoelectric acoustic-electric power feedthru for metal walls," *Proc. SPIE*, vol. 6930, Mar. 2008, Art. no. 69300Z.
- [10] D. A. Shoudy et al., "An ultrasonic through-wall communication system with power harvesting," in *Proc. IEEE Ultrasonics Symp.*, 2007, pp. 1848–1853.
- [11] J. D. Ashdown et al., "A full-duplex ultrasonic through-wall communication and power delivery system," *IEEE Trans. Ultrason., Ferroelectr., Freq. Control*, vol. 60, no. 3, pp. 587–595, Mar. 2013.
- [12] T. J. Lawry, K. R. Wilt, J. D. Ashdown, H. A. Scarton, and G. J. Saulnier, "A high-performance ultrasonic system for the simultaneous transmission of data and power through solid metal barriers," *IEEE Trans. Ultrason., Ferroelectr., Freq. Control*, vol. 60, no. 1, pp. 194–203, Jan. 2013.
- [13] K. R. Wilt, H. A. Scarton, G. J. Saulnier, T. J. Lawry, and J. D. Ashdown, "High-power operation of acoustic-electric power feedthroughs through thick metallic barriers," in *Proc. ASME Int. Mech. Eng. Congr. Expo.*, Oct. 2013, pp. 475–482.
- [14] M. Kluge, J. Sabater, J. Schalk, L. V. Ngo, H. Seidel, and U. Schmid, "Wireless sensing of physical parameters inside hermetically enclosed conductive envelopes," in *Proc. ASME Int. Des. Eng. Tech. Conf. Comput. Inf. Eng. Conf. Amer. Soc. Mech. Engineers Digit. Collection*, 2007, pp. 353–359.
- [15] O. Freychet, F. Frassati, S. Boisseau, N. Garraud, P. Gasnier, and G. Despesse, "Analytical optimization of piezoelectric acoustic power transfer systems," *Eng. Res. Exp.*, vol. 2, no. 4, Nov. 2020, Art. no. 045022.
- [16] T. J. Winnard, "Theoretical parametric study of through-wall acoustic energy transfer systems," M.S. thesis, Virginia Tech, Blacksburg, VA, USA, May 2021.
- [17] H. F. Leung and A. P. Hu, "Modeling the contact interface of ultrasonic power transfer system based on mechanical and electrical equivalence," *IEEE Trans. Emerg. Sel. Topics Power Electron.*, vol. 6, no. 2, pp. 800–811, Jun. 2018.
- [18] O. Freychet et al., "A versatile through-metal-wall acoustic power and data transfer solution," in *Proc. 19th Int. Conf. Micro Nanotechnol. Power Gener. Energy Convers. Appl.*, 2019, pp. 1–6.
- [19] S. Moss et al., "Modelling and experimental validation of the acoustic electric feedthrough technique," Air Vehicles Division, Defence Sci. Technol. Organisation, Victoria, Australia, DSTO-RR-0338, 2008.
- [20] K. R. Wilt, T. J. Lawry, H. A. Scarton, and G. J. Saulnier, "One-dimensional pressure transfer models for acoustic/electric transmission channels," *J. Sound Vib.*, vol. 352, pp. 158–173, Sep. 2015.
- [21] H. Yang, M. Wu, Z. Yu, and J. Yang, "An ultrasonic through-metal-wall power transfer system with regulated DC output," *Appl. Sci.*, vol. 8, no. 5, May 2018, Art. no. 692.
- [22] V. F.-G. Tseng, S. S. Bedair, and N. Lazarus, "Acoustic power transfer and communication with a wireless sensor embedded within metal," *IEEE Sensors J.*, vol. 18, no. 13, pp. 5550–5558, Jul. 2018.

- [23] T. J. Lawry, K. R. Wilt, H. A. Scarton, and G. J. Saulnier, "Analytical modeling of a sandwiched plate piezoelectric transformer-based acoustic-electric transmission channel," *IEEE Trans. Ultrason., Ferroelectr., Freq. Control*, vol. 59, no. 11, pp. 2476–2486, Nov. 2012.
- [24] S. Moss, J. Skippen, M. Konak, I. Powlesland, and S. Galea, "Detachable acoustic electric feedthrough," *Proc. SPIE*, vol. 7647, Apr. 2010, Art. no. 764745.
- [25] H. F. Leung, B. J. Willis, and A. P. Hu, "Wireless electric power transfer based on acoustic energy through conductive media," in *Proc. 9th IEEE Conf. Ind. Electron. Appl.*, 2014, pp. 1555–1560.
- [26] H. F. Leung and A. P. Hu, "Modeling and analysis of ultrasonic power transfer system with tightly coupled solid medium," *Wireless Power Transfer*, vol. 4, no. 1, pp. 1–12, Mar. 2017.
- [27] G. S. Kino, *Acoustic Waves: Devices, Imaging, and Analog Signal Processing*. Englewood Cliffs, NJ, USA: Prentice-Hall, Jan. 1987.
- [28] D. T. Blackstock, *Fundamentals of Physical Acoustics*. Hoboken, NJ, USA: Wiley, Apr. 2000.
- [29] K. Ono, "A comprehensive report on ultrasonic attenuation of engineering materials, including metals, ceramics, polymers, fiber-reinforced composites, wood, and rocks," *Appl. Sci.*, vol. 10, no. 7, Jan. 2020, Art. no. 2230.
- [30] M. Gorostiaga, M. C. Wapler, and U. Wallrabe, "Analytic model for ultrasonic energy receivers and their optimal electric loads II: Experimental validation," *Smart Mater. Struct.*, vol. 26, no. 10, 2017, Art. no. 105021.
- [31] M. Castillo, P. Acevedo, and E. Moreno, "KLM model for lossy piezoelectric transducers," *Ultrasonics*, vol. 41, no. 8, pp. 671–679, Nov. 2003.
- [32] M. Wild, M. Bring, E. Halvorsen, L. Hoff, and K. Hjelmervik, "The challenge of distinguishing mechanical, electrical and piezoelectric losses," *J. Acoustical Soc. America*, vol. 144, no. 4, pp. 2128–2134, Oct. 2018.
- [33] C. H. Sherman and J. L. Butler, *Transducers and Arrays for Underwater Sound*. New York, NY, USA: Springer, 2007.
- [34] D. Frickey, "Conversions between S, Z, Y, H, ABCD, and T parameters which are valid for complex source and load impedances," *IEEE Trans. Microw. Theory Techn.*, vol. 42, no. 2, pp. 205–211, Feb. 1994.
- [35] D. M. Pozar, *Microwave Engineering*, 4th ed. Hoboken, NJ, USA: Wiley, Dec. 2011.
- [36] D. Anderson, "Comparison of spice vs. harmonic balance simulations," in *Proc. 55th ARFTG Conf. Dig.*, 2000, vol. 37, pp. 1–7.



Ahmed Allam received the Ph.D. degree in mechanical engineering from the Georgia Institute of Technology, Atlanta, GA, USA, in 2021.

He is currently a Postdoctoral Fellow with the Smart Structures and Dynamical Systems Laboratory, Georgia Tech, Atlanta, GA, USA. He authored more than seven journal papers and multiple conference proceedings on active and passive acoustic metamaterials, phononic crystals, ultrasonic power transfer, sound energy harvesting, piezoelectric transducer design, and ultrasonic nondestructive testing.



Christian L. Arrington received the M.S. degree in materials engineering from the NM Institute of Mining and Technology, Socorro, NM, USA, in 2013.

He is currently a Principal Member of Technical Staff with Sandia National Labs, Multi Scale Fabrication, Science, and Technology Development Group and leads the Metal Micromachining Program. He has 21 years expertise leveraging electro-chemical deposition (ECD), metal coatings, ECD of binary and tertiary alloy-based

metals, traditional UV lithography, deep X-Ray lithography (LIGA), CMP, metrology, and multilayer semiconductor processing. He has been a part of two R&D 100 award winning teams at Sandia, has six patents/patent applications, and 36 publications. He was the Primary Investigator for microfabrication projects targeting: ion trap microfabrication for quantum science, phase contrast imaging grating fabrication, artificial retinal implant devices, radiation detection sensors, microfluidics, and superconducting device fabrication.



Christopher St. John received the B.S. degree in chemical engineering from New Mexico State University, Las Cruces, NM, USA, in 2009.

He is currently a Principal Technologist with the Multiscale Fabrication Development Department, Sandia National Laboratories, where he is involved with several research projects involving applications of mechanical transduction, electrochemistry, and materials science. He has presented and coauthored conference proceedings and articles on highly magnetostrictive electroformed resonators, ion trap fabrication, electroplated microcalorimeter detectors, electrochemical endpoint detection, and copper electrodeposition of blind through-silicon vias. He is also a published author in the world of sabermetrics



Jeffrey Steinfeldt received the bachelor's degree in microelectronic engineering from the Rochester Institute of Technology of Rochester, Rochester, NY, USA, in 2004.

He was with the Intel Corporation, Santa Clara, CA, USA, CTS, Lisle, IL, USA, and SoIAero/Emcore, in various process and yield engineering roles. He is an inventor on more than 20 patents

Mr. Steinfeldt was the recipient of the IEEE student design contest.



Alper Erturk received the Ph.D. degree in engineering mechanics from Virginia Tech, Blacksburg, VA, USA, in 2009.

He is currently the Woodruff Professor with the G. W. Woodruff School of Mechanical Engineering, Georgia Institute of Technology, Atlanta, GA, USA, where he leads the Smart Structures and Dynamical Systems Laboratory. He has authored or coauthored two books and more than 250 papers in journals and conference proceedings on dynamics, vibration, and acoustics of passive and active structures (with more than 17 000 citations and h-index of 59).

Prof. Erturk is a Fellow of ASME and SPIE. He is a recipient of various awards, including the NSF CAREER Award, ASME Gary Anderson Early Achievement Award, ASME C. D. Mote Jr. Early Career Award, and SEM J. W. Dally Young Investigator Award, among others.



Ihab El-Kady received the B.Sc. degree in physics from Cairo University, Giza, Egypt, in 1993, and the M.S. and Ph.D. degrees in condensed matter physics from the Iowa State University of Science and Technology, Ames, IA, USA, in 1999 and 2002, respectively.

At Iowa State University of Science and Technology, he studied computational electrodynamics, wave propagation in complex media, photonic crystals, plasmonics, and metamaterials. He is currently a Distinguished Member of Technical Staff with the Applied Photonic Microsystems Department, Sandia National Laboratories, Albuquerque, NM, USA. While with Sandia, led the development of the seminal award winning group theory based inverse design MIRaGE Toolkit. He is the lead Sandia National Laboratory investigator on the mechanical transduction of data and power through sealed barriers. He holds 19 issued patents, 26 patent applications, more than 226 publications, and 30 invited talks. He is currently leading several research projects including nano-scale photonics and phononics, metamaterials, micro-scale thermal transport, thermoelectrics, and optomechanics. As a Principal Member of Technical Staff, he developed the Group theory methodology for inverse design of metamaterials based on symmetry analysis. As a Staff member, he was the Principal Investigator of several internally funded research projects.

He is currently a Distinguished Member of Technical Staff with the Applied Photonic Microsystems Department, Sandia National Laboratories, Albuquerque, NM, USA. While with Sandia, led the development of the seminal award winning group theory based inverse design MIRaGE Toolkit. He is the lead Sandia National Laboratory investigator on the mechanical transduction of data and power through sealed barriers. He holds 19 issued patents, 26 patent applications, more than 226 publications, and 30 invited talks. He is currently leading several research projects including nano-scale photonics and phononics, metamaterials, micro-scale thermal transport, thermoelectrics, and optomechanics. As a Principal Member of Technical Staff, he developed the Group theory methodology for inverse design of metamaterials based on symmetry analysis. As a Staff member, he was the Principal Investigator of several internally funded research projects.